

# Methods for segmenting curved needles in ultrasound images

Stephen H. Okazawa, Richelle Ebrahimi, Jason Chuang,  
Robert N. Rohling \*, Septimiu E. Salcudean \*

*Department of Electrical and Computer Engineering, University of British Columbia, 2332 Main Mall, Vancouver, BC, Canada V6T 1Z4*

Received 24 December 2005; accepted 4 January 2006

Available online 7 March 2006

## Abstract

Ultrasound-guided percutaneous needle insertions are widely used techniques in current clinical practice. Some of these procedures have a high degree of difficulty because of poor observability of the needle in the ultrasound image. There have been recent efforts to improve guidance by computer assisted needle detection. These software techniques are often limited by not representing needle curvature. We present two methods to detect the needle in 2D ultrasound that specifically address needle curvature. Firstly, we demonstrate a real-time needle segmentation algorithm based on the Hough transform which detects the needle and represents its curved shape. Secondly, we demonstrate how a new coordinate transformation can transform detection of a curved needle to a linear fit. These methods are demonstrated on ultrasound and photographic images.

© 2006 Elsevier B.V. All rights reserved.

**Keywords:** Needle segmentation; Ultrasound; Needle biopsy; Percutaneous procedures

## 1. Introduction

Minimally invasive percutaneous procedures under image guidance have a wide variety of applications in the fields of medical diagnostics and therapeutics. These procedures employ long, fine needles to access remote targets in the patient's body percutaneously, i.e., via a puncture through the skin. Biopsy and drug delivery are typical applications where percutaneous techniques are frequently used. Compared to equivalent clinical interventions performed under open surgery, percutaneous needle punctures are fast, inexpensive, and minimize patient trauma. Unlike open surgery, a percutaneous approach will never involve direct observation of the target tissue. Therefore, in most cases some form of medical imaging technology is employed to locate the target and to guide the needle to this location. Of these technologies, 2D ultrasound is

common because of its minimal equipment and real-time display.

In practice, the target, such as a lesion suspected of being cancerous, may reside deeply within the body and may be adjacent to organs and tissues sensitive to injury. This makes precise needle placement of critical importance, but such precision is generally difficult to achieve. Because of the combination of poor image quality, the two-dimensional limitations in US imaging, and the flexibility of the fine needles used in these procedures, trial and error still plays a substantial role in reaching the target.

During percutaneous interventions, the behavior of the needle over the course of the insertion is difficult to predict and a perfectly straight line insertion cannot be assumed (DiMaio and Salcudean, 2003). Lateral forces acting on the bevelled needle tip and heterogeneous tissue properties deflect the needle from its apparent axis at the needle base. Needles have also been invented that can intentionally follow curved trajectories (Okazawa et al., 2005; Salcudean et al., 2002). Hence, accurate and up-to-date knowledge of the needle position during the insertion is essential to guide the needle and to confirm that the needle tip has

\* Corresponding authors. Tel.: +1 604 822 2045; fax: +1 604 822 5949.  
E-mail addresses: [rohling@ece.ubc.ca](mailto:rohling@ece.ubc.ca) (R.N. Rohling), [tims@ece.ubc.ca](mailto:tims@ece.ubc.ca) (S.E. Salcudean).

reached the target. While ultrasound provides a real-time, cross-sectional image to help guide the needle, maintaining good needle visualization is challenging. Ultrasound signal noise, shadows, and other artifacts obscure the appearance of the needle (Huber et al., 2001). Augmenting the detection and visualization of the needle would ease the challenges associated with these procedures.

Passive methods of improving needle visualization in ultrasound include physical modification of the needle tip by mechanical scoring and chemical coatings (Charboneau et al., 1990). These modifications improve the needle's ultrasound reflectivity, brightening its appearance in the ultrasound image.

Active methods to improve needle visibility include adaptive beam steering of the ultrasound array to enhance the reflections from the needle (Cheung and Rohling, 2004), and miniature magnetic sensors embedded in the needle tip (Glossop et al., 2002).

Software algorithms that automatically segment the needle from the rest of the ultrasound image have been the subject of recent research. Draper et al. (2000) have developed an ultrasound needle segmentation algorithm which overlays the computed needle position on the US display to help the physician track the needle. This technique employs a general bright-line search algorithm using statistical methods to identify linear features.

We have previously explored needle segmentation (Ebrahimi et al., 2003) using a similar method and found that the approach was computationally demanding and that correct segmentation failed in certain situations where the location of the needle was still detectable by the naked eye. The basic approach initially processed the image using a median filter for speckle removal and a thresholding operation. The resulting binary image was composed of scattered groups of pixels some of which were part of the needle image. We then calculated the correlation coefficient of each pixel group and certain combinations of pixel groups in order to segment the strongest line-like feature. Problems arose firstly because building the lists of each group's member pixels was computationally expensive and the speed of this step was unpredictable. Secondly, in some cases, noise and other image artifacts caused the needle to appear broken into a series of many disconnected bright spots. In such situations, the thresholding operation produced binary images in which the needle was composed of many small groups along its shaft. Taken individually, these small groups contained virtually no information about the needle's overall shape, hence, the needle segmentation algorithm was unable to abstract the needle image from the pixel data.

To overcome this difficulty, linear feature detection based on the Hough transform can be used (Hough, 1962) because it considers the overall image and is less sensitive to noise. In other words, the main advantage is the ability to detect line features that may be partially occluded by shadows, speckle and signal-fallout that is typical of ultrasound. For example, computer vision techniques to

link edge elements from gradient edge detection would likely fail because of large gaps in the appearance of the needle. The Hough transform also has an inherent mechanism to reject other linear features in the image that are not part of the needle. This is based on the search for a peak in the accumulator, as explained in Section 2.

The standard Hough method for line detection transforms the entire cartesian image space to a slope-intercept coordinate frame by exhaustively projecting the image pixels in all directions (with some specified angular resolution) between 0° and 180°. The Hough transform is robust, but computationally demanding. Ding and Fenster (2003) have developed a performance-optimized needle segmentation algorithm using the Hough transform that segments a needle in real-time ultrasound imaging. Similar software needle segmentation techniques have also been applied to 3D ultrasound (Smith et al., 2001; Ding et al., 2003).

Because these previous needle detection algorithms are based on linear-feature detection methods, the potential for needle curvature is usually ignored. Artifacts often hide or distort the appearance of the needle and needle tip. Yet the ability to localize the needle is very important to the physician.

A great deal of literature exists on the theory, use and extension of the Hough Transform. A summary is given by Illingworth and Kittler (1988) with more recent work summarized by Leavers (1993). The problem of rapid line or curve detection in noisy images occurs in many fields and both specialized and generalized methods have been proposed. For example, linear generalized Hough transform (LIGHT) by Li et al. (1993) demonstrates improved robustness to noise and partial occlusions. Grimson and Huttenlochner (1990) and Shapiro (1975), among others, have also studied the effects of noise, localization errors and detectability. Davies (1990) uses Sobel edge detection to reduce the dimensionality of the problem and increase speed. Leavers (1992) also looks at curves (using more than the two parameters needed for straight lines) by first mapping to a 2D space for line detection then passing the results to second stage.

In this paper, we present two new specialized techniques to detect a curved needle in 2D ultrasound images. Although most of the previous work on Hough transforms for curve detection is on non-medical applications, some aspects are adapted to our problem.

The first technique employs a novel line-detection method, a Hough transform, and a polynomial regression to segment mildly curved needles. While the techniques mentioned above employ general line search algorithms that detect lines of any position and orientation, we use a reduced search field based on approximate knowledge of needle position and orientation which can be roughly predicted for a given needle insertion. This substantially reduces the number of Hough projections that must be performed. Ding and Fenster (2003) use an initial thresholding step and perform the Hough Transform on the reduced data set of the resulting binary image. Our line-detection step

supplies the Hough Transform with a smaller data set in which the needle data is predominant. Finally, the line detected by the Hough transform is used to define a narrow window within which a polynomial regression fits a curve to the needle data, thus capturing mildly curved trajectories.

As the needle curvature increases, the applicability of the first method is diminished. We present the mathematics of a second needle segmentation algorithm that formally addresses highly curved needle trajectories. For this purpose, we have developed an extension to the Hough transform step which adds a curvature parameter to the slope-intercept coordinate system. The curvature parameter is based on an empirical model for needle bending behavior in tissue. In this new coordinate space, lines in the original image, either straight or curved, that conform to our needle bending model can be extracted and described by their slope, intercept, and radius of curvature.

## 2. Hough transform-based curved needle detection

This needle segmentation algorithm is fundamentally based on an edge-detection and Hough transform approach to identify the best needle candidate in the ultrasound image. As a consequence of using the Hough-transform for line-feature detection, we assume here that the needle will be the longest and straightest feature in the image, despite the fact that the needle may be mildly curved. However, we want to represent this needle curvature, not a linear approximation thereof. Therefore, the best straight-line candidate for the needle determined by the Hough transform is used to define a narrow window within which points discovered by the edge-detection step are expected to fall on the real needle shaft. This remaining data are fit to a curve using a polynomial regression and overlaid upon the ultrasound image in real-time.

Though desirable, performing the standard Hough transform over the whole ultrasound image is not feasible for real-time image processing on current personal computer (PC) hardware. Typically, some image pre-processing is performed to reduce the data set that is transformed to slope-intercept coordinates. Ding and Fenster (2003) use a thresholding operation for this purpose. However, because the needle tends to appear as a sharp-edged feature, we process the original image using an edge detection approach. We have explored a technique that searches for the characteristic gradient cross-section of a bright line feature with a specified thickness so that we can tune the line-detection to the needle width. In this way, we transform to slope-intercept coordinates only a small set of data in which we have a high level of confidence that the needle data is predominant. Existing line detection techniques used in ultrasound or other applications subject to speckle are general line detectors or line enhancers (Czerwinski et al., 1998), whereas our approach is to capitalize on specific prior knowledge of the approximate orientation and thickness of the needle image to aid in its segmentation in real-time.

### 2.1. Algorithm steps

A summary of the algorithm is provided below. Before starting, the width of the probe, the depth setting and the side of needle insertion (left or right) is used to determine the maximum range of possible needle angles. This range limits the region of interest (ROI) to perform the search. The gauge of the needle is also assumed to be known.

1. Choose a rough approximation of the needle's axis line in the ultrasound image based on the expected trajectory and define a rectangular ROI.
2. Cast a multitude of rays perpendicular to the approximate needle line within the ROI. These rays should cross the needle shaft at roughly right angles. The approximate needle axis, ROI, and perpendicular rays are shown in Fig. 1.
3. For each pixel along each ray, calculate the average pixel intensity among that pixel and a line of neighboring pixels parallel to the approximate needle line. The neighborhood of pixels is shown in Fig. 2. This step filters out noise and any bright features that are not part of a line running roughly parallel to the approximate needle line.
4. For each pixel along each ray, calculate the linear derivative along the ray of the averaged pixel intensities. We use the simplest approximation for the derivative using the following equation,

$$\frac{d}{dn} i[n] \approx i[n+1] - i[n], \quad (1)$$

where  $i[n]$  is the averaged pixel intensity of the  $n$ th pixel along the ray.

This is the edge-detection step. Sharp edges in the ultrasound image that are crossed by the rays will appear as peaks. The first side of the needle shaft crossed by the ray will produce a positive peak and

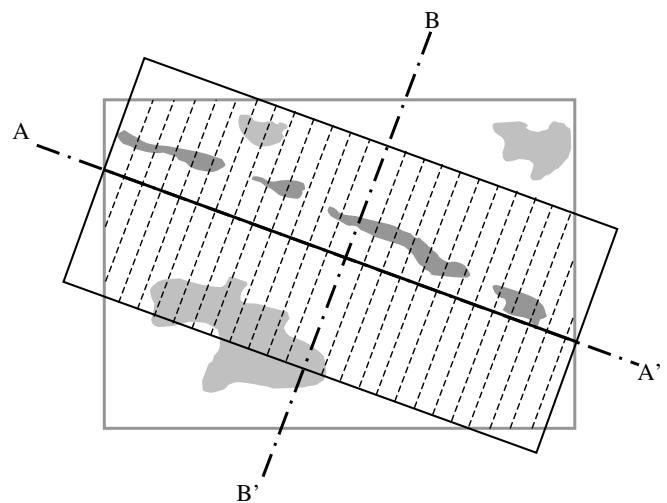


Fig. 1. Illustration of an ultrasound image (shown in shades of gray) with the approximate needle axis (black line) oriented along A–A' and perpendicular rays (dashed lines) oriented along B–B'.

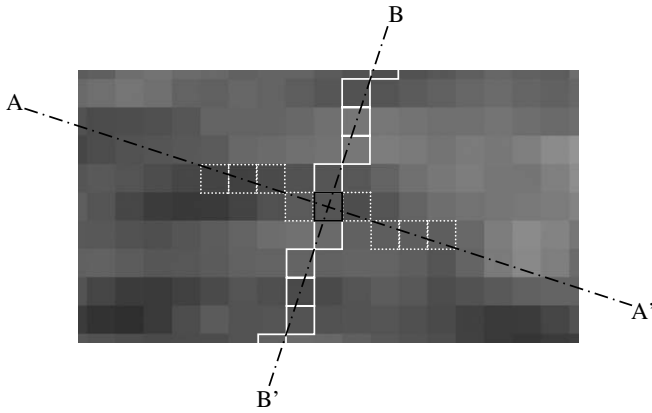


Fig. 2. Pixel intensity averaging step in which the intensity of a given pixel (black outline) along a B–B' oriented ray (white outline) is averaged among its neighboring pixels (white, dashed outline) along an A–A' oriented line parallel to the approximate needle axis.

the second side will produce a negative peak. Indeed, this approximation to the derivative results in a noisy derivative profile but subsequent steps have the effect of averaging this data.

5. Traverse each ray looking at a window of derivative values along the ray, and search for a derivative profile across the window that matches that of the needle. The size of the window is a parameter which is set to approximately the width of the needle as it appears in the ultrasound image. Fig. 3 shows derivative values along a ray and the window positioned over a needle-like derivative profile. Moving along each ray in increments of one pixel, compute the value of *score* using the following equation,

$$\text{score} = S_{\text{lag}} - S_{\text{lead}} - |S_{\text{lag}} + S_{\text{lead}}|, \quad (2)$$

where  $S_{\text{lead}}$  is the sum of the derivative values in the leading half of the window and  $S_{\text{lag}}$  is sum of the derivative values in the lagging half of the window, as shown in Fig. 3. The summing of derivative values within the window-halves filters the noise generated by the derivative performed in the previous step.

When the window is centered on the needle shaft,  $S_{\text{lag}}$  will be large and positive and  $S_{\text{lead}}$  will be large and negative resulting in a large positive *score*. All other derivative profiles will result in a lower (more negative) *score*. The  $|S_{\text{lag}} + S_{\text{lead}}|$  term penalizes the *score* if  $S_{\text{lag}}$  and  $S_{\text{lead}}$  are not approximately equivalent in magnitude, i.e., if we have a sharp edge but not a finite width needle.

For the window position that produced the highest *score* along each ray, record the position of the pixel at the window center. This is the best guess at where the needle shaft crosses each ray.

6. Project all the points from the previous step along the approximate needle line and accumulate their *score* values in an array of bins that span the width of the ROI. The bin location with the highest accumulated *score* defines the strongest linear feature parallel to the approximate needle line of this iteration. Fig. 4 shows the projection step and the *score* histogram. This is the line detection technique derived from the Hough transform.

Because we are quantizing the needle point positions into bins, we smooth the accumulated bin scores by adding the current pixel's *score* to the appropriate bin and half that *score* to each of its neighboring bins. This prevents a strong linear feature from being

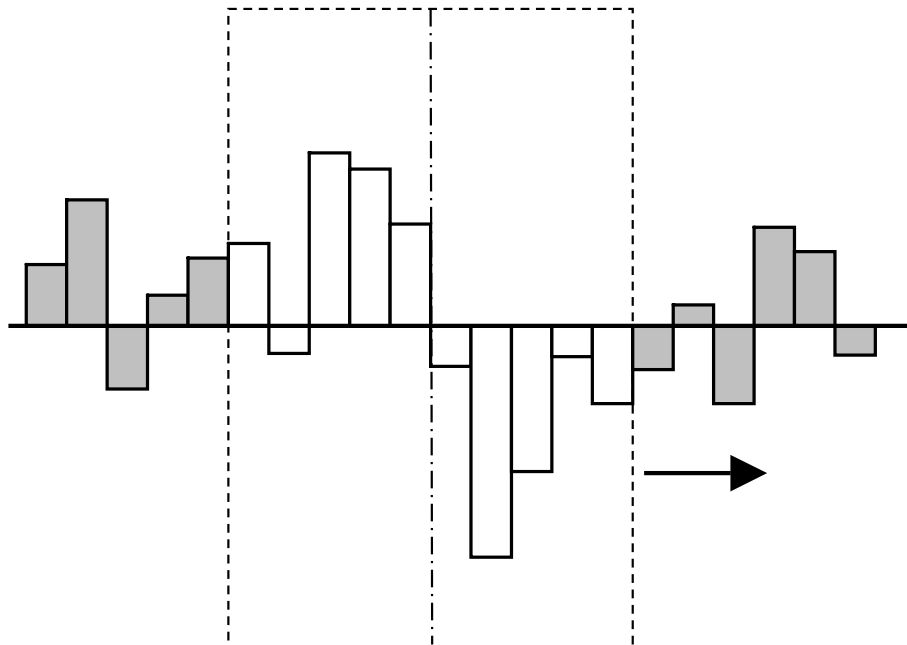


Fig. 3. Derivative values along a ray showing the window positioned over a needle-like feature where the leading half of the window is to the right, and the lagging half of the window is to the left.

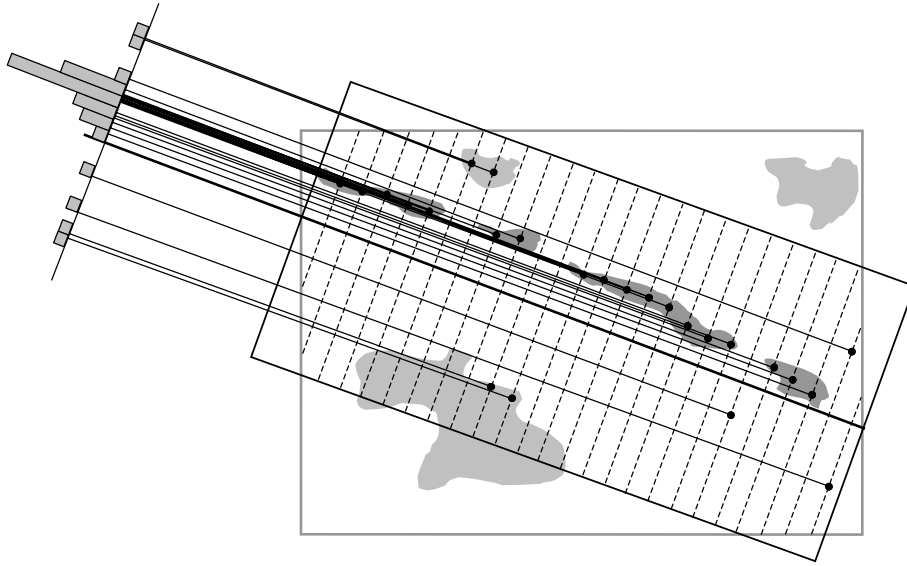


Fig. 4. Illustration of the selected needle points along each ray and the projection of needle point scores along the approximate needle axis in order to detect the strongest linear feature parallel to the axis.

missed if it lies on the boundary between two bins causing its *scores* to be split between the two.

7. Rotate the initial linear approximation of the needle by a small angular increment and repeat steps 2–7 until the angular search range has been exhausted. Record the set of data points for the iteration that produced the largest accumulated bin *score*. The line parallel to the approximate needle line for that iteration that passes through the highest scoring bin position defines the best linear guess for the needle.

8. Reject points whose distance from the best linear guess exceeds a threshold value. We want to include all the points that contributed to the largest peak in the bin *scores* and reject those points that form a part of other image features.
9. Fit the remaining points to a polynomial equation using a polynomial least squares regression.
10. Define the tip of the needle using the deepest detected point. Fig. 5 shows the best linear representation of the needle, the point rejection thresholds, and the final polynomial representation of the needle up to the tip.

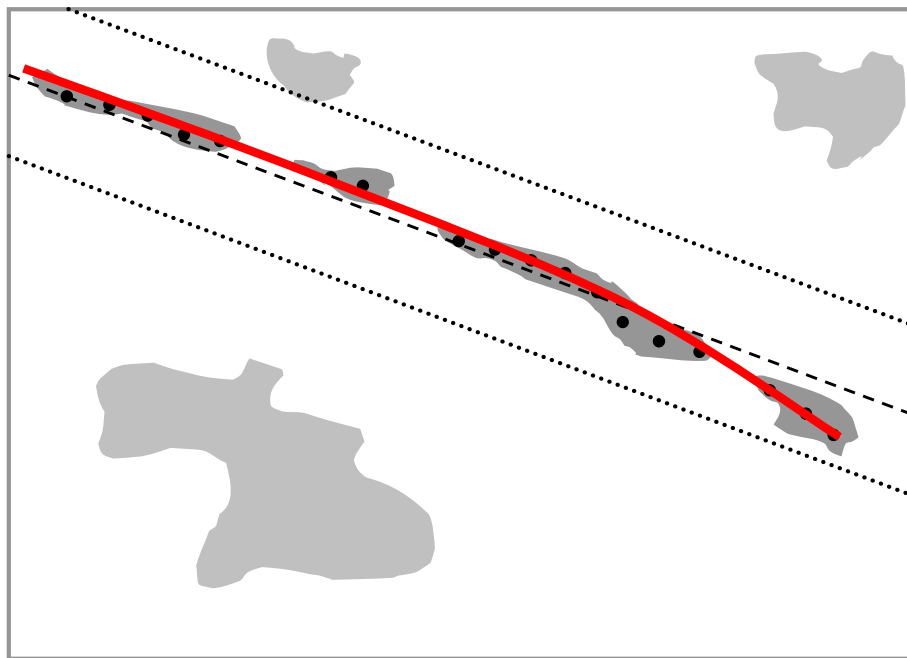


Fig. 5. Illustration of the final polynomial representation of the needle (red line) also showing the best linear representation of the needle (dashed line) and the point rejection thresholds (dotted lines). (For interpretation of the references to colour in this figure legend, the reader is referred to the web version of this article.)



## 2.2. Implementation and method illustration

Implementation of the needle segmentation algorithm was performed on the Ultrasonix 500RP ultrasound machine (Ultrasonix Medical Corporation, Burnaby, Canada). The 500RP is a commercial PC-based ultrasound machine with a software developer's kit that allows real-time access to the entire imaging pipeline and system configuration variables. The machine runs on dual 1.5 GHz pentium processors and 512 Mbytes of RAM. This hardware was able to run both the ultrasound software and the needle segmentation algorithm in real-time. The software was developed in C++ using Intel's Pentium-optimized Integrated Performance Primitives (Intel Corporation, Santa Clara, CA) for image processing tasks. The transducer is a 38 mm linear array transducer with a frequency range of 4–9 MHz. The Model 52 Ultrasound Needle Biopsy Phantom (CIRS Inc. Norfolk, VA) was used to test the algorithm on simulated breast tissue. The phantom contains both cystic and solid masses in a realistic tissue-mimicking medium.

Given an image of  $482 \times 398$  pixels, the width of the ROI is set to 300 pixels. The length of the ROI extends to the edges of the ultrasound image. As shown in Fig. 6, these ROI dimensions encompasses the majority of the ultrasound image. For each iteration we use 40 perpendicular rays spaced uniformly across the length of the ROI. Ten repetitions are performed by incrementing the slope of the ROI across an approximate  $\pm 15^\circ$  angular range. The pixel intensity averaging step is performed within a neighborhood consisting of the line of four adjacent pixels

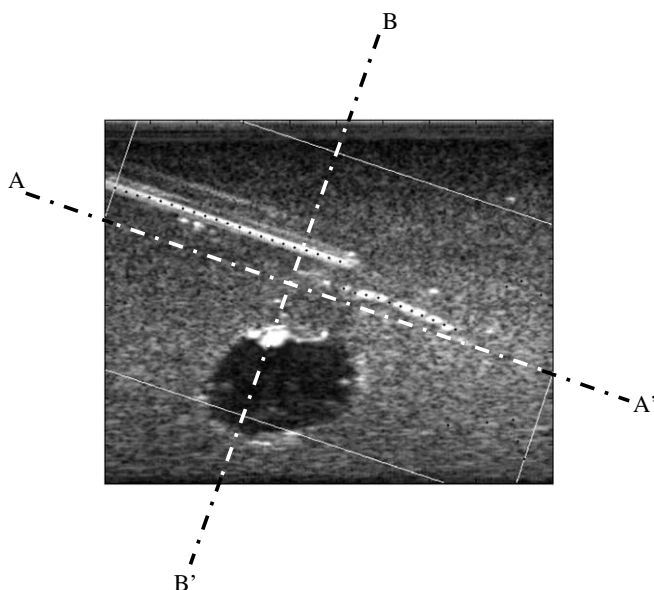


Fig. 6. Results of the line detection step showing the highest scoring points along each ray (black dots). Note that the disconnected bright line segment above and to the right of the dark mass is not part of the needle but is a feature of the tissue that resembles the needle. The threshold performed in step 8 of the algorithm will ultimately remove these data points.

on either side of the current pixel along the ray. The window size used to traverse each ray has a length of 10 pixels. This value is chosen to reflect the cross-sectional size of the needle image in the ultrasound display. The choice of window size is discussed further below. For the Hough transform projection step, an array of 20 bins evenly spaced across the width of the ROI is used. The outlier rejection step, which follows the identification of the best linear approximation of the needle, employs a threshold distance of 10 pixels. (Further relaxing this threshold distance in trying to capture more strongly curved needles would eventually fail because the Hough transform step is programmed to detect only linear features.) Within this region, a third order polynomial regression is used to represent the true needle shape which may be mildly curved. Given this set of parameters, a frame rate of 17 frames per second was achieved for the needle detection algorithm.

Fig. 6 shows the highest scoring points along each ray in a sample ultrasound image. We can see that the points do center on the most needle-like linear features that cross each ray with a high success rate. Fig. 7 shows the pixel intensity and pixel *score* profiles along one of the rays in Fig. 6. The plots illustrate how the window scoring method is sensitive only to bright features that have the correct width. In effect, the window size is an upper bound on the detectable line width. Line features whose cross-sections are larger than the window are considered to be too wide to be the needle and will not score as highly as lines whose width is narrower than the window. Therefore, the window width is set to approximately the largest needle diameter that we expect to observe in the ultrasound display. In practice, the location of the needle with respect to the focal point had no appreciable effect, and we were able to tune the window size parameter to work for a variety of typical needle gauge sizes.

Fig. 8 demonstrates needle detection in a variety of poor conditions where the image of the needle is broken and distorted by shadows and artifacts. The algorithm is not confused by the presence of nearby sharp bright features. Detection of the needle tip, however, remains a difficulty with this technique. Every ray in the ROI will locate a point that most closely resembles a needle shaft whether or not the needle has penetrated deeply enough to cross that ray. It is difficult to define a threshold to eliminate those points whose *score* is not high enough to be considered part of the needle. Image brightness and contrast and the relative brightness of the needle are very inconsistent from one procedure to the next. Therefore, a reliable image processing solution to needle tip localization may not be possible.

The use of a polynomial least-squares regression to define the detected needle shape has the potential to produce a highly improbable needle trajectory if only a few data points are used. We cannot totally eliminate this possibility. However, if the number of data points that remain after the final outlier rejection step is too small, we determine that the needle segmentation attempt for this frame

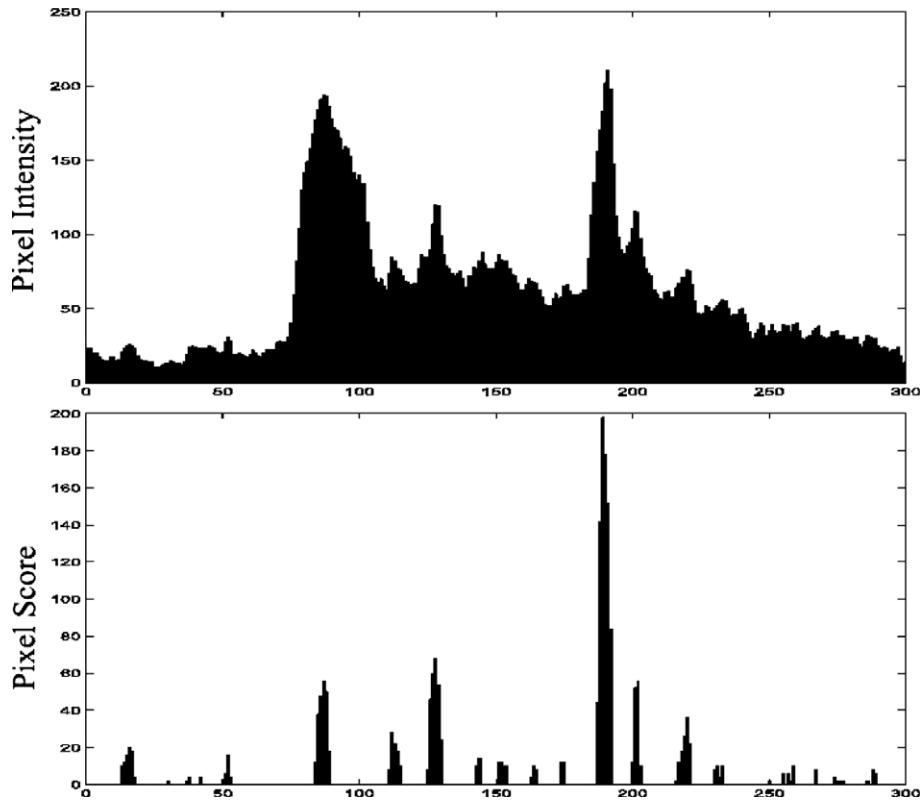


Fig. 7. Pixel intensity and pixel *score* profiles are calculated along the B'–B aligned ray in Fig. 6. The profiles are calculated only for pixels inside the ROI. The scoring method assigns a higher *score* to the second large peak in the intensity profile because its width more closely matches that of a needle.

has failed and no overlay is drawn. The polynomial can also become ill-defined if the needle orientation is near vertical. The polynomial should therefore be defined with respect to the coordinate system that is approximately aligned with the needle, so that fold-over can never occur.

### 3. Coordinate transform-based needle segmentation

The preceding needle segmentation algorithm assumes that the image of the needle in the ultrasound display will be the longest and straightest line feature. The effectiveness of the algorithm breaks down if the needle is substantially curved. However, the bending behavior of the needle in tissue can be predicted to fall within a range of feasible bent shapes that can be described mathematically. By quantifying the bent state of the needle with a new parameter, we have developed a technique that maps the original image to a new three-dimensional space from which we can extract the slope, intercept, and curvature parameters of line features. This generalized approach allows us to detect lines which are not necessarily straight but which conform to an empirical model for needle bending.

#### 3.1. Formulation of the coordinate transform

When a lateral force acts on the tip of the needle (such as that due to the needle tip bevel) the resulting curvature can

be approximated by an arc of constant radius. Fig. 9 shows the vector field formed by paths of constant radius emanating from a common point and slope. The actual bent needle path shown in the figure conforms nicely to this field of theoretical paths.

We define an inclined rectangular ROI such that the needle enters the ROI parallel to the length of the rectangle and at the center of its width. The local Cartesian image coordinates  $U$  and  $V$  describe pixel positions inside this ROI with the origin at the point where the needle enters the ROI. The  $U$ -axis is aligned to the rectangle's length, and the  $V$ -axis is aligned to its width.

The relationship between a point  $(p_u, p_v)$  in the  $UV$ -plane to its equivalent point  $(p_x, p_y)$  in the original image ( $XY$ -plane) is described by the following expression,

$$\begin{pmatrix} p_x \\ p_y \end{pmatrix} = R \begin{pmatrix} p_u \\ p_v \end{pmatrix} + \begin{pmatrix} o_x \\ o_y \end{pmatrix}, \quad (3)$$

where  $R$  is the rotation matrix for inclined angle of the ROI and the point  $(o_x, o_y)$  is the location of the  $UV$ -plane origin in the original image.

The curved paths that make up the field of possible needle trajectories are arcs of constant radii. We parameterize points in this fan-shaped area of mathematically described needle trajectories with the two variables  $M$  and  $N$ . The variable  $M$  is the arc length (insertion depth) to the point from the origin, and the variable  $N$  is the reciprocal of

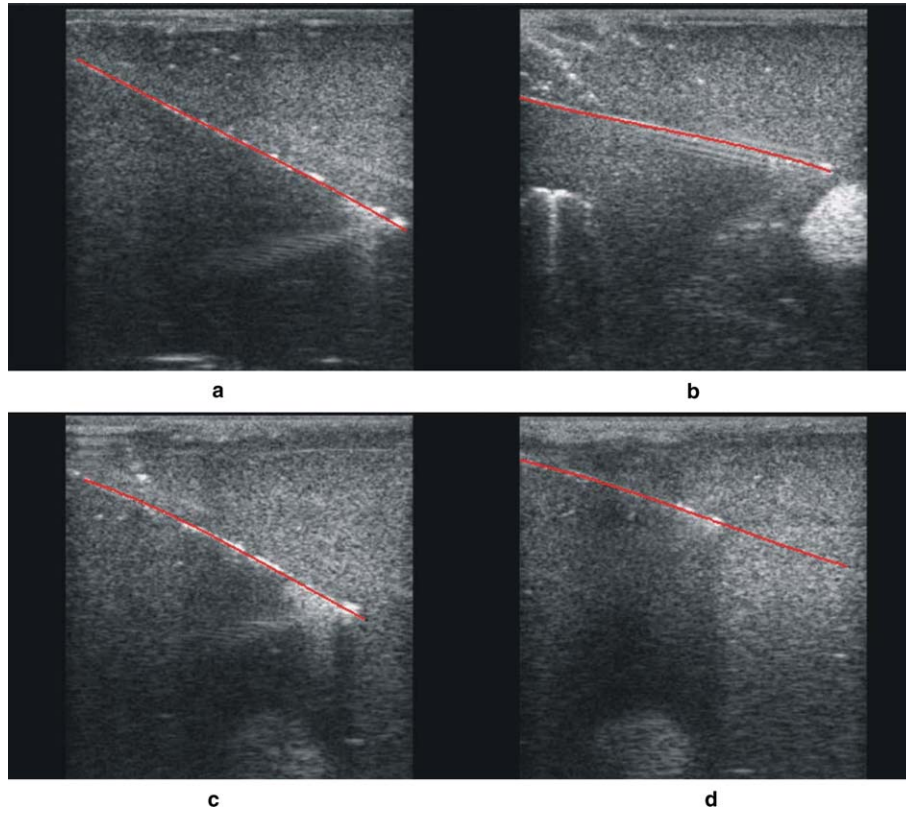


Fig. 8. Real-time needle segmentation results showing: (a) successful detection of a poor needle image with only bright spots visible along the needle shaft and strong artifacts at the needle tip; (b) successful detection of a faint needle image with many other sharp, bright features present; (c) successful detection of a needle image made up of several disconnected bright pieces with strong artifacts and a mild downward curve; and (d) correct needle shaft detection but failed needle tip detection.

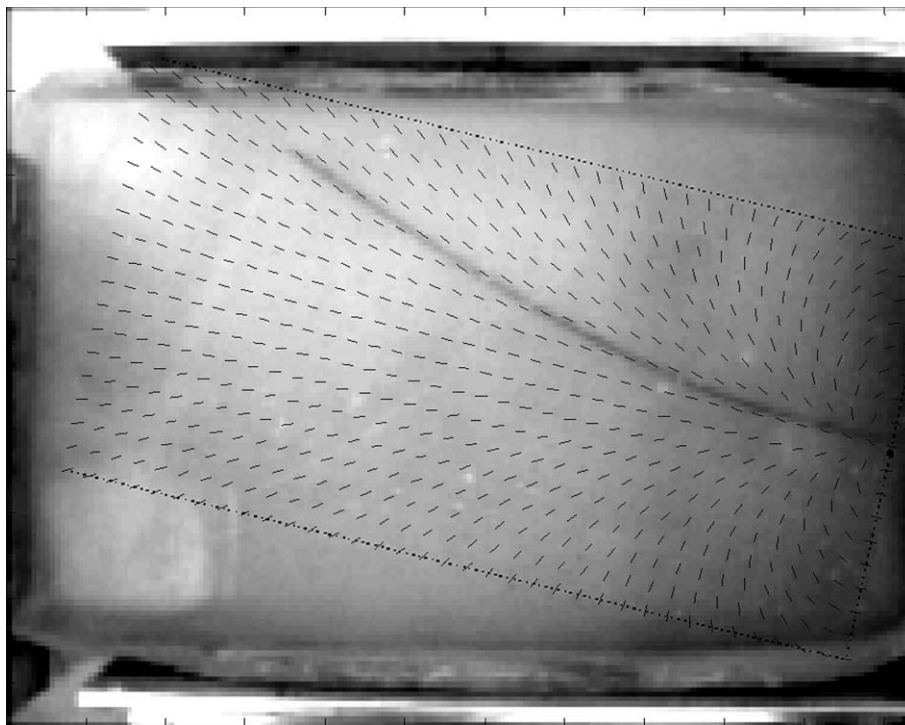


Fig. 9. The field of theoretical needle path directions inside the  $UV$ -plane.



the radius of curvature for the arc that passes through that point.

The arcs defined by the needle curvature parameters  $M$  and  $N$  may be expressed in  $UV$  coordinates by the following complex equation ( $i = \sqrt{-1}$ ),

$$U + i \cdot V = \frac{i}{N} (1 - e^{i \cdot M \cdot N}). \quad (4)$$

The conversion from points in the  $UV$ -plane to the  $MN$ -plane is then

$$N = \frac{1}{r}, \quad (5)$$

$$M = |r| \cdot a \tan 2 \left( \frac{U}{r - V} \right), \quad (6)$$

where

$$r = \frac{U^2 + V^2}{2 \cdot V}. \quad (7)$$

A needle-like feature in the ultrasound image will be detected when the following three conditions are met: (1) the needle shaft passes through the  $UV$ -plane origin, (2) the slope of the needle shaft at the  $UV$ -plane origin equals the slope of the  $U$ -axis, and (3) the needle lies along an arc described by a unique  $N$ -value. These three conditions represent the three coordinates of the image transformation: intercept, slope, and curvature, respectively.

### 3.2. Algorithm steps

1. Choose a rough approximation of the needle's axis line in the ultrasound image based on the expected trajectory.
2. Define a rectangular ROI around the approximate needle line assuming it will always contain the needle during the procedure. This defines the  $UV$ -plane.
3. Within the ROI, compute edge magnitude and orientation using Sobel edge detector masks.
4. Select pixels as possible needle points if the edge magnitude is greater than a certain threshold and if the edge orientation is within  $\pm 15^\circ$  from the ideal edge orientation.

Fig. 9 illustrates the ideal angle field in the  $UV$ -plane. The ideal edge angle at a pixel ( $U, V$ ) is given by  $2 \cdot \arctan(V/U)$ .

5. Map the selected points from the  $UV$ -plane to the  $MN$ -plane using equations (5)–(7). A series of points that form an arc of constant radius originating at the  $UV$ -plane origin parallel to the  $U$ -axis will appear as a horizontal line (constant  $N$ -value) in the  $MN$ -plane. See Fig. 10.

Techniques for approximating the needle as a straight line may now be applied to fit a needle path to the data. A variety of different robust line-fitting methods could be employed with similar results. The key is to observe that large variance in  $N$ -value for points near the  $UV$ -plane origin (where arc of all radii converge) compared to points

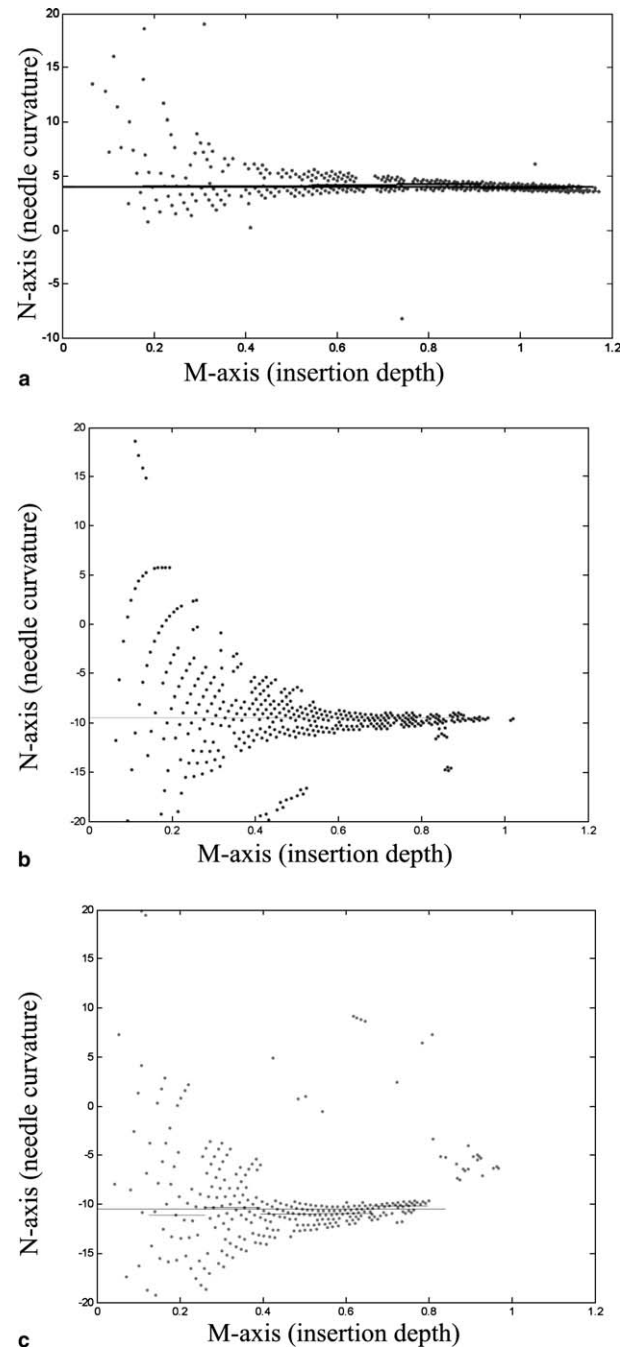


Fig. 10. Plot of the selected points from the edge detection step mapped to the the  $MN$ -plane (dots), along with the best fit (lines). Figs. (a)–(c) correspond to (a)–(c) in Fig. 11.

near the needle tip. This is due to the nature of the  $UV$  to  $MN$  coordinate transformation where  $N = 1/r$ .

6. The approach chosen here is to divide the  $M$ -axis into five uniform regions and compute the median  $N$ -value of the data points in each region. In this way, the needle is represented with five points whose  $M$ -value equals the mid-point of the region and whose  $N$ -value equals the median  $N$ -value of the data points in that region. Finally, compute the best-fit horizontal line through the five points obtained above using a least squares

technique. This defines the  $N$ -value for the ideal needle arc that most closely matches the selected points for this iteration.

7. Repeat steps 2–6 while changing both the position and orientation of the  $UV$ -plane in small increments until the positional and angular search ranges are exhausted. The position of the  $UV$ -plane origin is varied along a line perpendicular to the first approximate needle axis. The coordinate mapping to the  $MN$ -plane only detects arcs that originate at the  $MN$ -plane origin with initial slope parallel to the  $U$ -axis. This is why we vary both orientation and position so that one such combination produces a  $UV$ -frame with its origin on the needle and the  $U$ -axis aligned with the needle at the origin. The trial that yields the minimum total variance in  $N$ -values for the selected points is chosen as the data set that best captures the needle shape.

The three most important things for a good fit are: (a) the detected  $N$  values should all lie close to the fitted  $N$  value, (b) there should be greater weight on  $N$  values that are closer to the needle tip (i.e., higher  $M$  value), and (c) there should be a large number of points detected in order to make the fit reliable. The variance is therefore calculated using the following:

$$\text{variance} = \sum_{i=1}^k (|n_i - N_{fi}| * m_i^2) / k^2, \quad (8)$$

where  $n$  is an array of the detected  $N$  values of size  $k$ ,  $N_f$  is the best fit  $N$  value, and  $m$  is an array of detected  $M$  values of the same length as  $n$ . The square terms were used to magnify the effect of errors near the tip and the effect of having a small number of detected points.

8. The position, orientation, and curvature of the detected needle is defined by the position and orientation of the  $UV$ -plane and the best-fit  $N$ -value for the chosen data set. In summary, this approach is a variation on the regular Hough transform method since it involves a calculation of the variance in the  $MN$ -plane for each position and orientation of the  $UV$ -plane.

### 3.3. Implementation and method illustration

The potential of this approach is first explored in a controlled experimental setting. A transparent tissue-mimicking phantom is constructed of a 1.5 cm thick polyvinyl chloride sheet 10 cm wide and 18 cm long. The modulus of elasticity of the phantom is approximately 100 kPa which is within the range of typical breast and prostate tissue (Krouskop et al., 1998). The phantom is mounted on a light table and photographs of needle insertions were taken from above with a digital camera. For the needle insertions, we used a standard medical biopsy needle with a modified stylet tip that is able to produce insertion trajectories of varying curvature that simulate real situations in which the needle does not track straight (Ebrahimi

et al., 2003). To demonstrate the capabilities of the three-dimensional parameter transformation, we applied the image processing techniques of this new needle segmentation algorithm to the photographic images taken in this experimental setup. For these experiments, pre-processing of the image prior to the transformation consists of standard edge detection techniques using the Sobel edge detector masks. The line detection technique used in the previous algorithm is suited to live ultrasound images and is not necessary for processing the photographs used to test the feasibility of this approach.

We see from Fig. 11, that a heavily curved trajectory produced in a controlled insertion experiment can be closely represented by this needle detection algorithm by processing the photographic images. Only minor errors between the true path and the detected arc are visible near the base and tip of the needle in Fig. 11(a) and (b). A slightly larger error is evident in Fig. 11(c) near the needle tip.

One source of error is that the needle curvature is not exactly constant-radius, as assumed by the algorithm. This is because the curvature of the needle has a mild depth

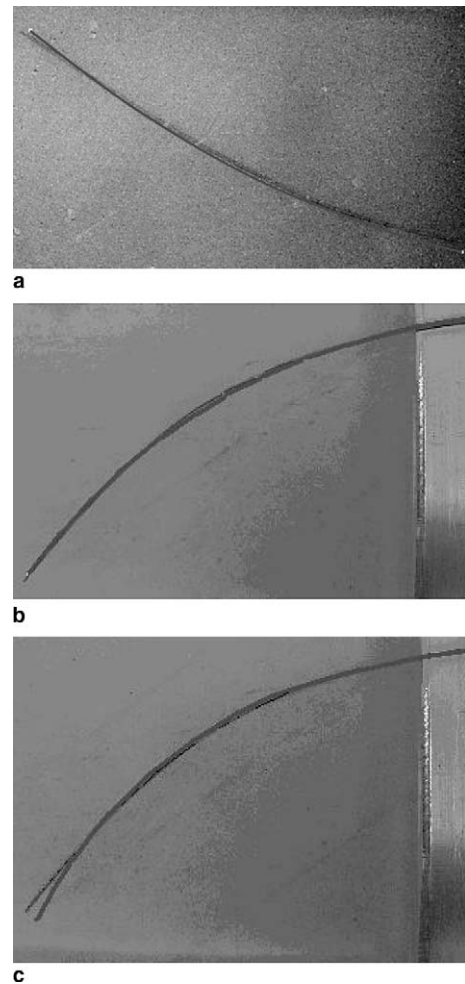


Fig. 11. The actual needle and the superimposed best fit curve. Figs. (a)–(c) correspond to (a)–(c) in Fig. 10.

dependency whereby the needle tends to bend more easily early in the insertion and less easily as the insertion depth increases. In practice, all needle trajectories cannot be expected to have a constant radius of curvature, and where deviations from a uniform curvature arise, errors between the true needle trajectory and the model will increase.

A second source of error is the presence of outliers that may cause a non-ideal fit to the data in step 8. In Fig. 11(c), the segment near the needle tip is affected by outliers visible near the top of Fig. 10(c). Nevertheless, the method is able to extract an arc that still matches the needle over most of its length, despite the high curvature, just as the

standard Hough transform extracts the line that most closely matches the needle data. We are therefore able to segment needles from images based on a broader and more accurate definition of what a needle is, namely, that it will be long, thin, and possibly curved in a manner that we define mathematically.

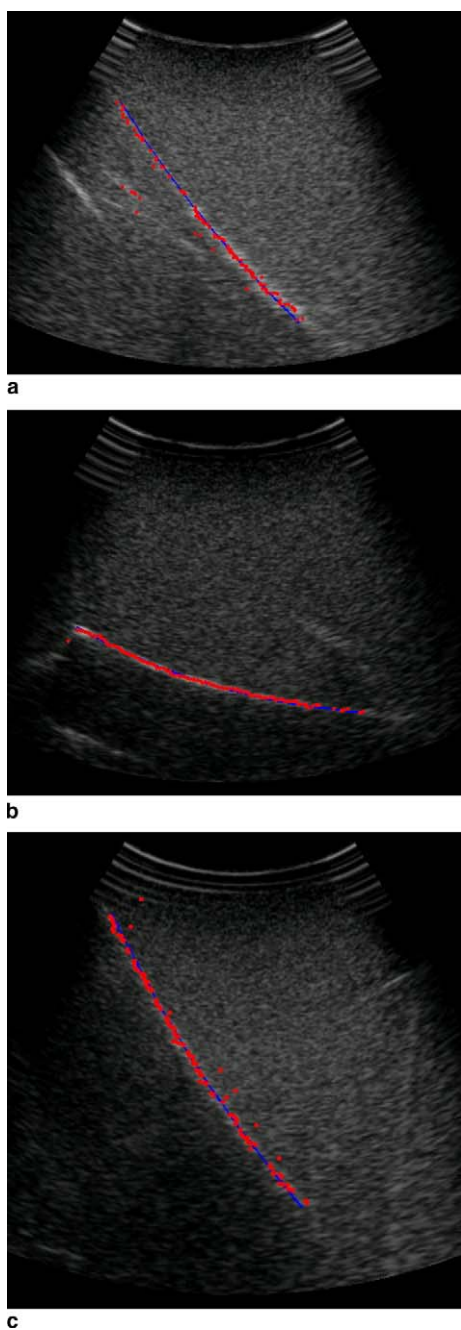


Fig. 12. The detected edges are shown as dots. These edges correspond to best fit lines shown in (a)–(c) of Fig. 13.

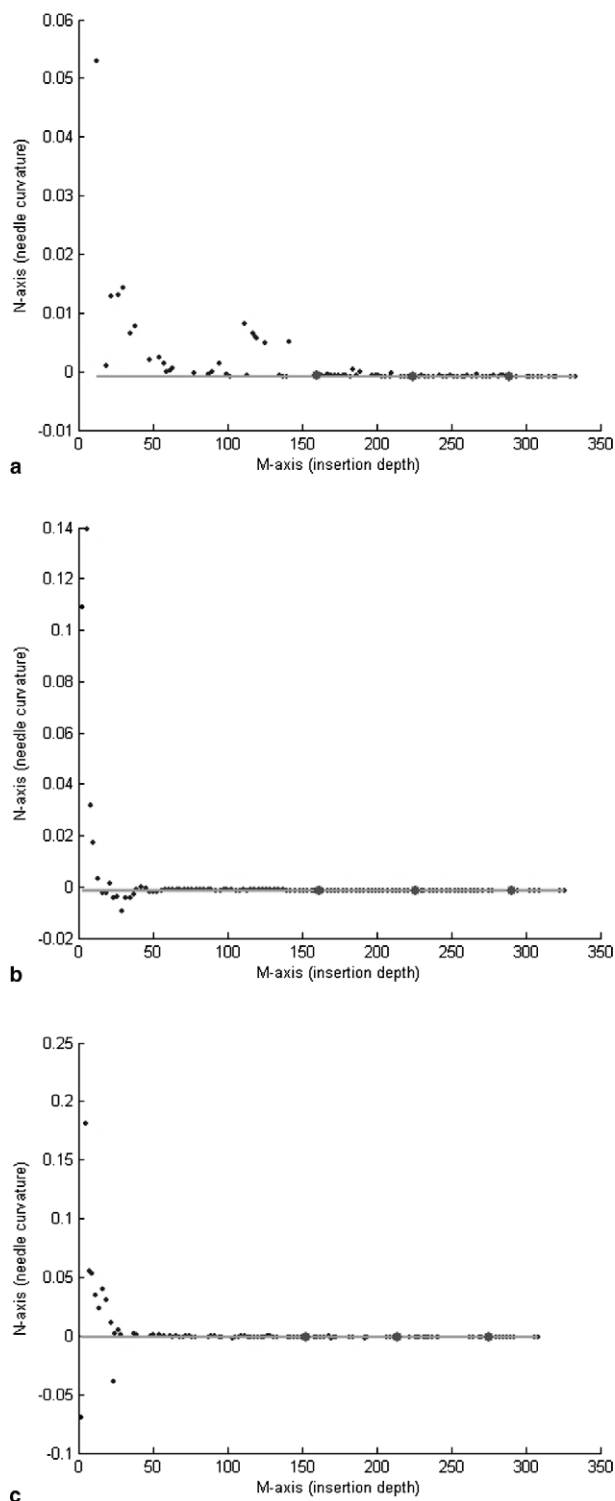
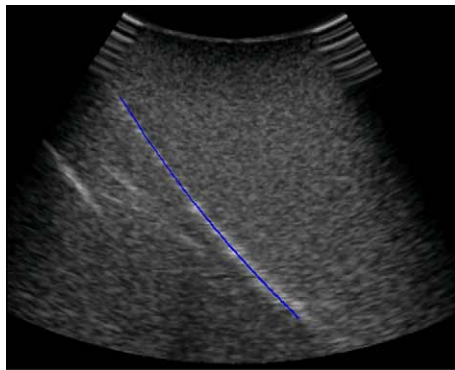
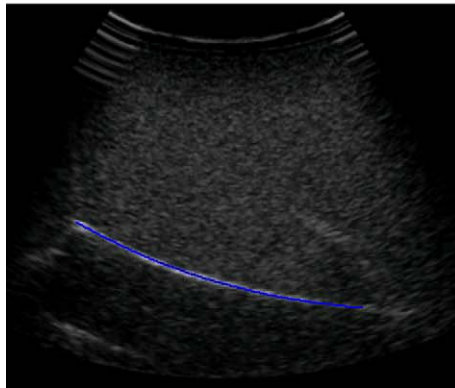


Fig. 13. Plot of the selected points from the edge detection step mapped to the  $MN$ -plane (dots), along with the best fit (lines). Figs. (a)–(c) correspond to (a)–(c) in Figs. 12 and 14.

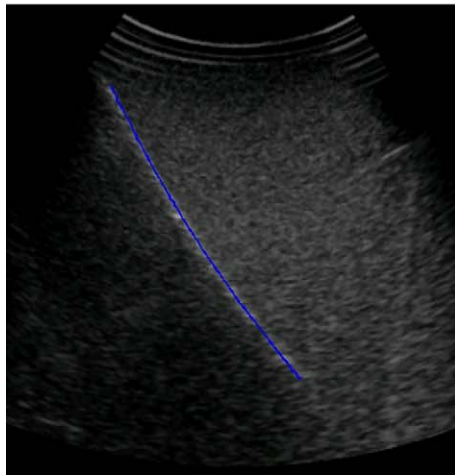
A second set of tests was performed on ultrasound images. Again a polyvinyl chloride sheet was constructed, this time with a stiffness of 50 kPa. A similar 18 gauge needle with a modified stylet was used to produce a curved trajectory. The needle was segmented using the complete algorithm described above in Section 3.2. The results from the ultrasound images are shown in Figs. 12–14. The algorithm was able to cope with the typical speckle and artifacts found in ultrasound.



a



b



c

Fig. 14. The actual needle and the superimposed best fit curve. Figs. (a)–(c) correspond to (a)–(c) in Figs. 12 and 13.

Table 1

Accuracy of the coordinate-transform based needle detection algorithm is calculated in 10 ultrasound images

Image	Tip deflection (mm)	Mean error (mm)	Maximum error (mm)	Perpendicular tip error (mm)	Tangential tip error (mm)
1	12.5	0.5	1.6	1.1	0.2
2	3.6	0.4	0.7	0.2	−0.2
3	4.3	0.2	0.6	0.2	1.7
4	5.5	0.2	0.7	0.1	0.5
5	9.7	0.2	0.6	0.2	12.1
6	16.4	0.3	0.8	0.8	8.2
7	3.2	0.3	1.1	0.5	0.0
8	12.2	0.5	1.1	0.4	0.2
9	1.4	0.3	0.6	0.4	−0.2
10	0.7	0.8	1.3	0.6	2.3

Tip deflection is a measure of the amount of needle curvature. The error is calculated between the automatic and manual measurements. The error is also divided into perpendicular (normal to the needle) and tangential errors.

The detected needle locations were compared with manual measurements for 10 needle insertions with various curvatures. The differences in locations are listed in Table 1. Curvature is measured here simply as the deviation of the tip from a straight line fit. In addition to mean and maximum errors calculated over the length of the needle, the error is broken into perpendicular and tangential components. This is done because some tests showed good accuracy perpendicularly, but poor accuracy tangentially. These cases arose when the needle trajectory was accurately detected by the segmentation algorithm, but the tip was poorly detected. Fig. 14 shows such a case.

Cases with poor tip detection occur when the needle curves away from the ultrasound probe resulting in poor reflection of the ultrasound echoes. This means the contrast of the needle is reduced and the needle is lost within the noise of the ultrasound image. The stronger appearance of the rest of the needle still allows the trajectory to be calculated with good accuracy in the perpendicular direction.

#### 4. Conclusion

We have demonstrated two new needle detection methods. The unique goal of the methods is to provide segmentation of curved needles. The first method uses a combination of a line-detection technique and the Hough transform to identify the needle. Further image processing allows us to capture the potentially curved shape of the real needle and to display this information on the ultrasound image in real-time. In some situations the needle will be substantially curved, and the linear feature detection capabilities of the standard Hough transform may not be effective in locating the needle. We have, therefore, proposed an enhancement to the Hough method that makes use of an empirical model for needle bending behavior in tissue. In this method, the ultrasound image data is mapped to a new three-parameter space from which we may extract

slope, intercept, and curvature parameters that describe an arcing trajectory that matches the needle. The mathematics of the approach have been described and validation performed on optical images where the true curvature is clearly visible. The results showed that the needle curvature is reasonably modelled as constant curvature.

Reliable estimation of the location of the needle tip remains a challenge with conventional ultrasound even with the new software methods. Future work will investigate the combination of these techniques with more robust tip detection methods. For example, purposeful vibration of the tip can be detected with Doppler ultrasound. Implementation of the algorithms for specific clinical applications is another goal. Biopsies of deep tissue and epidural anesthesia are two such clinical applications. Additional work will also combine the steerable needle with these methods for the long term goal of computer-based trajectory control.

### Acknowledgements

This work was supported by the Natural Sciences and Engineering Research Council of Canada (NSERC). Thanks also to Adam Harmat for help with coding and testing.

### References

- Charboneau, J.W., Reading, C.C., Welch, T.J., 1990. CT and sonographically guided needle biopsy: current techniques and new innovations. *American Journal of Roentgenology* 154, 1–10.
- Cheung, S., Rohling, R., 2004. Enhancement of needle visibility in ultrasound guided percutaneous procedures. *Ultrasound in Medicine and Biology* 30 (5), 617–624.
- Czerwinski, R.N., Jones, D.L., O'Brian Jr., W.D., 1998. Line and boundary detection in speckle images. *IEEE Transactions on Image Processing* 7 (12), 1700–1714.
- Davies, E.R., 1990. *Machine Vision*. Academic Press, New York.
- DiMaio, S.P., Salcudean, S.E., 2003. Needle Steering and Model-Based Trajectory Planning. In: *Proceedings of the MICCAI 2003*, vol. 2878, LNCS, pp. 33–40.
- Ding, M., Fenster, A., 2003. A real-time biopsy needle segmentation technique using Hough transform. *Medical Physics* 30 (8), 2222–2233.
- Ding, M., Cardinal, H.N., Fenster, A., 2003. Automatic needle segmentation in three-dimensional ultrasound images using two orthogonal two-dimensional image projections. *Medical Physics* 30 (2), 222–234.
- Draper, K.J., Blake, C.C., Gowman, L., Downey, D.B., Fenster, A., 2000. An algorithm for automatic needle localization in ultrasound-guided breast biopsies. *Medical Physics* 27 (8), 1971–1979.
- Ebrahimi, R., Okazawa, S., Rohling, R., Salcudean, S.E., 2003. Hand-Held Steerable Needle Device. In: *Proceedings of MICCAI 2003*, vol. 2879, LNCS, pp. 223–230.
- Glossop, N.D., Cleary, K., Kull, L., Banovac, F., 2002. Needle tracking using the aurora magnetic position sensor. In: *CAOS 2002*, Santa Fe, USA, June 2002.
- Grimson, W.E.L., Huttenlochner, D.P., 1990. On the sensitivity of the Hough transform for object recognition. *IEEE Transactions on Pattern Analysis and Machine Intelligence* 10 (3), 255–274.
- Hough, P.V.C. Method and means for recognizing complex patterns. US Patent 3,069,654. December 18, 1962.
- Huber, S., Wagner, M., Medl, M., Czembirek, H., 2001. Real-time spatial compound imaging in breast ultrasound. *Ultrasound in Medicine and Biology* 28 (2), 155–163.
- Illingworth, J., Kittler, J., 1988. A survey of the Hough transform. *Computer Vision Graphics and Image Processing* 44, 87–116.
- Krouskop, T.A., Wheeler, T.M., Kallel, F., Garra, B.S., Hall, T., 1998. Elastic moduli of breast and prostate tissue under compression. *Ultrasonic Imaging* 20, 260–274.
- Leavers, V.F., 1992. Use of the Radon transform as a means of extracting symbolic representations of shape in two dimensions. *Image Vision Computing* 10 (2), 99–107.
- Leavers, V.F., 1993. Which Hough transform? *Computer, Vision Graphics and Image Processing* 58 (2), 250–264.
- Li, Z.N., Yao, B., Tong, F., 1993. Linear generalized Hough transform and its parallelization. *Image Vision Computing* 11 (1), 11–24.
- Okazawa, S., Ebrahimi, R., Chuang, J., Rohling, R., Salcudean, S.E., 2005. Hand-held steerable needle device. *IEEE/ASME Trans. Mechatronics* 10 (3), 285–296.
- Salcudean, S.E., Rohling, R.N., Okazawa, S.H., Ebrahimi, A.R., 2002. Steerable needle and guidance system. US Provisional Patent Application 60/435,263. December 23, 2002.
- Shapiro, S.D., 1975. Transformations for the computer detection of curves in noisy pictures. *Computers Graphics and Image Processing* 4, 328–338.
- Smith, W.L., Surry, K.J.M., Mills, G.R., Downy, D.B., Fenster, A., 2001. Three-dimensional ultrasound-guided core needle breast biopsy. *Ultrasound in Medicine and Biology* 27 (8), 1025–1034.